Paper Number: **47**

Title: **Validation of a Mesoscale Fiber Kinking Model through Test and Analysis of Double Edge Notch Compression Specimens**

Authors: Andrew C. Bergan
Wade C. Jackson

ABSTRACT

Tests and analyses were conducted on a series of geometrically-scaled double edge notch compression specimens to validate the capability of the fiber-kinking model in the NASA continuum damage mechanics code for progressive damage analysis, CompDam. The tests and analyses focused on the fiber-kinking damage mechanism, which is of critical importance for predicting accurately longitudinal compression failure in carbon fiber reinforced polymer laminates. The fiber-kinking model in CompDam was augmented with a new capability to represent a hardening response once a kink band has fully formed, enabling prediction of band broadening. Correlation of the test and analysis results showed agreement in stiffness and strength with less than 10% error. The analysis predicts the same sequence of events leading to ultimate failure that was found in the test. The overall excellent correlation in terms of stiffness, strength, and failure process validates the capability of the model for predicting longitudinal compression failure in notched laminates with cross-ply layups.

INTRODUCTION

One factor limiting the accuracy of predictions by many progressive damage analysis (PDA) codes for compression failures of carbon epoxy reinforced polymer laminates is that the physical characteristics of the fiber-kinking process are often ignored. The conventional continuum damage mechanics PDA approach uses the same phenomenological model in longitudinal compression and tension despite differences in the failure process [1,2].

The fiber-kinking theory introduced by Budiansky offers a physics-based model for kink band initiation and propagation [3,4]. Recently, a model based on this fiber-kinking theory was proposed and implemented into the NASA continuum damage mechanics code for PDA, CompDam [5]. A mesoscale model was formulated with consideration for the kinematics of fiber kinking, including shear instability and a post-peak non-zero

Andrew C Bergan, Structural Mechanics and Concepts Branch, NASA Langley Research Center, Mail Stop 190, Hampton, VA 23681, U.S.A.
Wade C. Jackson, Damage Tolerance, Durability, and Reliability Branch, NASA Langley Research Center, Mail Stop 190, Hampton, VA 23681, U.S.A.

residual stress. The model was verified through detailed comparisons with a high-fidelity micromechanical model and an analysis of an unnotched unidirectional coupon subjected to compression. One factor that was not explored in reference [5] is the response under large deformations, after kink band initiation. Furthermore, only limited validation of the model was conducted. Therefore, additional model development effort is needed.

In this paper, a detailed validation study of the PDA code CompDam for prediction of longitudinal compression failure in double edge notch compression (DENC) specimens is described. The paper is organized as follows. First, the experimental procedure utilized for testing a series of geometrically scaled DENC specimens, inspired by [6], is summarized. Next, the CompDam fiber-kinking model described in [5] is summarized, and a simple extension is introduced to consider hardening in the constitutive response after a kink band has formed. Finally, the test and analysis results are presented and discussed. Particular attention is given to correlation between the observed and predicted failure process in order to validate the model capabilities.

EXPERIMENTAL PROCEDURE

Specimen Configuration

Specimens were obtained from plates that were fabricated by hand layup of IM7/8552 carbon/epoxy prepreg plies and cured in an autoclave. The specimens were cut from a $[(90/0)_8/90/(0/90)_8]$ laminate using a waterjet. The average cured laminate thickness was t_L = 6.141 mm such that the average cured ply thickness was t_{ply} = 0.186 mm. The loading surfaces were ground flat and parallel. The DENC configuration with a notch length to width ratio a/w = 0.6 is shown in Figure 1. Specimens of nine sizes were fabricated by scaling the parameter w, yielding the dimensions summarized in Table I. Each size was assigned a capital letter designation from 'A' through 'I'. Three or four replicates were tested for each size.

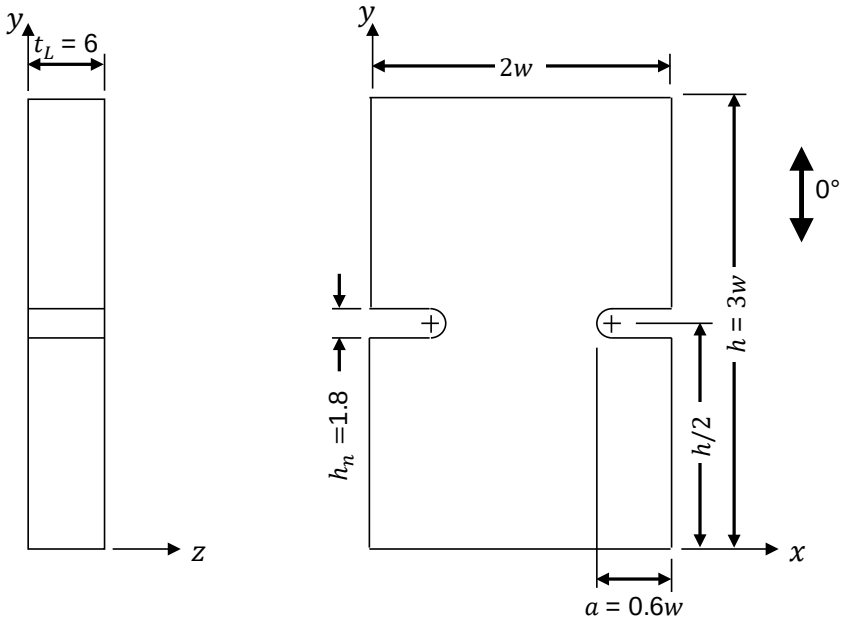

Figure 1. Test specimen configuration (dimensions in mm).

TABLE I. DENC SPECIMEN DIMENSIONS.

	Size designation								
	A	B	C	D	E	F	G	H	I
w [mm]	5	7.5	10	12.5	15	17.6	20	22.5	25
h [mm]	15	22.5	30	37.5	45	52.5	60	67.5	75
a [mm]	3	4.5	6	7.5	9	10.5	12	13.5	15

The front and back of the specimens were painted with a speckle pattern for digital image correlation (DIC) with the speckles appropriately sized for the field of view, which encompassed the entire specimen. A baseline ultrasound of each DENC specimen was conducted to identify any manufacturing-induced defects.

Test Setup

The specimens were loaded between hardened platens using a servo-hydraulic 100-kN test stand under displacement control. A photograph of the test setup for a 'B' specimen is shown in Figure 2. Loading was applied quasi-statically at a rate of 0.1 mm/min. A thin coating of molybdenum disulphide was applied between the specimen and loading platen to minimize friction.

Two DIC systems were used to monitor strains on the front ($z = t_L$) and back surfaces ($z = 0$) in real time during the tests. A third DIC system was used to monitor the loading platens to characterize rigid body rotation. Four of the six DIC cameras are visible in Figure 2 and are labeled. DIC image capture was synchronized for all six cameras and set to occur at 1 Hz. The load was recorded with each set of images throughout the loading history.

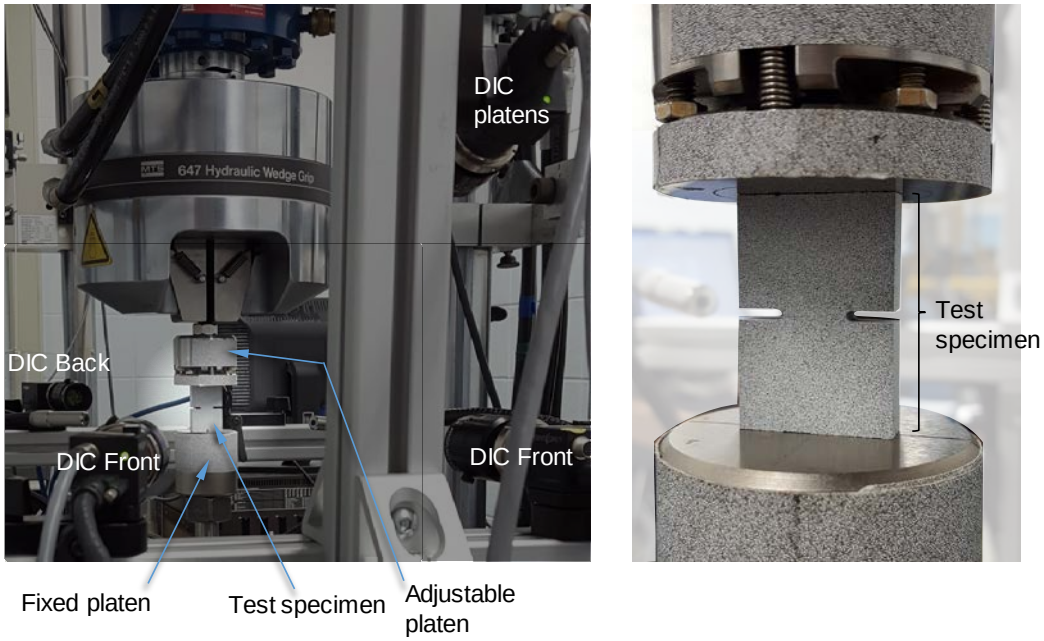

Figure 2. Experimental test setup showing (a) the test specimen, loading platens, and DIC cameras and (b) a zoomed-in view of the test specimen between the two loading platens.

All three DIC systems utilized five megapixel cameras. The field of view for the two DIC systems focused on the specimen was adjusted to the different specimen sizes to include the entire specimen in the field of view while maximizing the resolution.

In order to ensure uniform introduction of load into the specimens, an adjustable platen was used. The adjustable platen used a spherical bearing to enable adjustment in two degrees of freedom as well as jacking screws to fix the platen in place during loading, as shown in Figure 2b. The loading platen was adjusted at the beginning of the test under a subcritical load by balancing front-to-back and left-to-right strains across the specimen based on the DIC data.

FINITE ELEMENT MODELING

Fiber-kinking theory (FKT) identifies the relevant mechanisms in kink band formation as a combination of an infinitely-wide band of initially misaligned fibers, nonlinear shear stress-strain behavior, and large fiber rotation [3,4,7]. FKT produces the characteristic constitutive law shown in Fig. 3a where, once the strength, X_C, is reached, the stress drops to a residual "crush stress" level. The kink band is idealized, as shown in Fig. 3b, with a fiber misalignment angle, φ, kink band angle, β, and kink band width, w_{kb}. If the shear nonlinearity follows a Ramberg-Osgood [8] behavior, $\gamma_{12} = (\tau + \alpha\tau_{12}^{\eta})/G_{12}$ in the plane of the ply, FKT predicts the strength as

$$X_C = \frac{G_{12}}{1 + \eta\alpha^{1/\eta}\left(\frac{G_{12}\varphi_0}{\eta - 1}\right)^{\frac{\eta-1}{\eta}}} \tag{1}$$

where G_{12} is the in-plane shear modulus, α and η define the shape of the shear stress-strain curve, and φ_0 is an initial fiber misalignment.

Budiansky [7] also addressed the crushing (residual) stress, σ_r, by considering the behavior at large fiber rotations to derive the expression

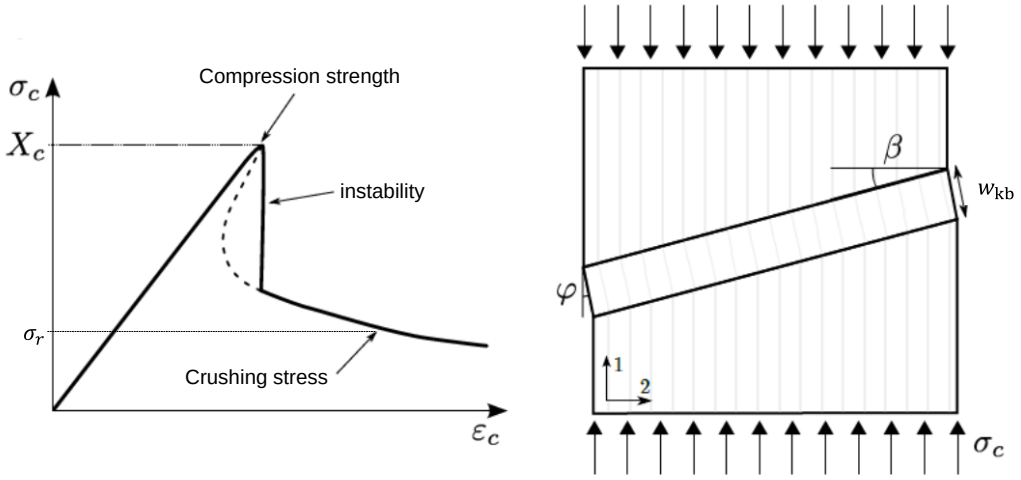

Figure 3. The (a) characteristic constitutive response predicted by fiber kinking theory and (b) idealization of the kink band.

$$\sigma_r = \frac{2\tau_L}{\sin 2\beta} \tag{2}$$

where τ_L is the shear stress associated with large rotations. While τ_L is somewhat arbitrary and no expression is given to determine β, by selecting τ_L and β based on experimental data, Eq. (2) provides an approximate value for the nonzero residual stress after a kink band has developed.

A constitutive model based on FKT (assuming $\beta = 0$) was recently proposed and implemented into the NASA continuum damage mechanics code for progressive damage analysis, CompDam [5,9]. This model is further developed by adding consideration for fiber failure in the post-peak portion of the constitutive response. The existing model and new developments are summarized in the following section.

Mesoscale Constitutive Model for Fiber Kinking

CONSTITUTIVE MODEL FORMULATION

The material model computes the stress state given the current deformation, state variables, and material properties as follows. Consider a material point with a reference frame, X_i. An initial fiber misalignment angle, φ_0, in the 1-2 plane, is assumed such that a fiber-aligned reference frame, X_i', is defined with rotation, $\boldsymbol{R}$, as

$$\boldsymbol{X'} = \boldsymbol{RX} \tag{3}$$

where

$$\boldsymbol{R} = \begin{bmatrix} \cos\varphi_0 & -\sin\varphi_0 & 0 \\ \sin\varphi_0 & \cos\varphi_0 & 0 \\ 0 & 0 & 1 \end{bmatrix} \tag{4}$$

The value of φ_0 can be determined by rearranging (1) as

$$\varphi_0 = \frac{\eta - 1}{G_{12}} \left(\frac{G_{12} - X_C}{X_C \eta \alpha^{1/\eta}} \right)^{\frac{\eta}{\eta - 1}} \tag{5}$$

For a given deformation, $\boldsymbol{F}$, the Green-Lagrange strain, $\boldsymbol{E}$, is calculated as

$$\boldsymbol{E} = \frac{1}{2}(\boldsymbol{F^T F} - \boldsymbol{I}) \tag{6}$$

Shear nonlinearity is accounted for in the $X_1' - X_2'$ plane using an uncoupled plasticity model based on the Ramberg-Osgood stress-strain law as follows

$$\boldsymbol{E'} = \boldsymbol{R^T E R} - \frac{\gamma_{12}^{PL}}{2} \begin{bmatrix} 0 & 1 & 0 \\ 1 & 0 & 0 \\ 0 & 0 & 0 \end{bmatrix} \tag{7}$$

where the plastic portion of the shear strain,

$$\gamma_{12}^{PL} = \gamma_{12} - \gamma_{12}^{EL} \tag{8}$$

is found iteratively using

$$\gamma_{12} = \frac{1}{G_{12}} [\tau_{12} + \text{sign}(\tau_{12}) \alpha |\tau_{12}|^{\eta}] \tag{9}$$

where τ_{12} is the shear stress and G_{12}, α, and η are the material properties that define the Ramberg-Osgood curve. As originally introduced in FKT, accounting for shear plasticity in the misaligned from in (7)–(9) captures large rotation of the fibers, which is the primary source of nonlinearity in the constitutive response. The second Piola-Kirchoff stress in the fiber-aligned reference frame, $\boldsymbol{S'}$, is calculated using the elastic stiffness tensor, $\mathbf{C}$

$$\boldsymbol{S'} = \mathbf{C}\colon \boldsymbol{E'} \tag{10}$$

with

$$\mathbf{C} = \mathbf{H^{-1}} \tag{11}$$

$$\mathbf{H} = \begin{bmatrix} \frac{1}{E_1^*} & \frac{-\nu_{21}}{E_2} & \frac{-\nu_{31}}{E_3} & 0 & 0 & 0 \\ \frac{-\nu_{12}}{E_1^*} & \frac{1}{E_2} & \frac{-\nu_{32}}{E_3} & 0 & 0 & 0 \\ \frac{-\nu_{13}}{E_1^*} & \frac{-\nu_{23}}{E_2} & \frac{1}{E_3} & 0 & 0 & 0 \\ 0 & 0 & 0 & \frac{1}{G_{23}} & 0 & 0 \\ 0 & 0 & 0 & 0 & \frac{1}{G_{13}} & 0 \\ 0 & 0 & 0 & 0 & 0 & \frac{1}{G_{12}} \end{bmatrix} \tag{12}$$

using the typical elastic constants. Fiber nonlinearity is accounted for following Kowalski [10] as

$$E_1^* = E_1(1 + c_l\varepsilon_{11}) \tag{13}$$

where c_l is the nonlinearity coefficient for the ply and is an additional material property to be obtained from test data. In the reference frame, $\boldsymbol{X}_i$, the second Piola-Kirchoff stress is

$$\boldsymbol{S} = \boldsymbol{R}\boldsymbol{S'}\boldsymbol{R^T} \tag{14}$$

Finally, the Cauchy stress is calculated.

$$\boldsymbol{\sigma} = \boldsymbol{F}\boldsymbol{S}\boldsymbol{F^T}|\boldsymbol{F}|^{-1} \tag{15}$$

This model was implemented in Abaqus/Explicit [11] as a VUMAT [9]. The following section describes special considerations for the post-peak response due to fiber breakage.

FIBER FAILURE

During the kinking process, large fiber rotation in the relatively short kink band width w_{kb} leads to high bending stresses in the fibers. As a result, it is typical for the fibers to break at the locations of maximum curvature (see, e.g., [12]). The result of these fiber breaks is the characteristic kink-band damage mode, typically observed post-mortem: an inclined band with broken fibers above and below short, high-rotated, fiber

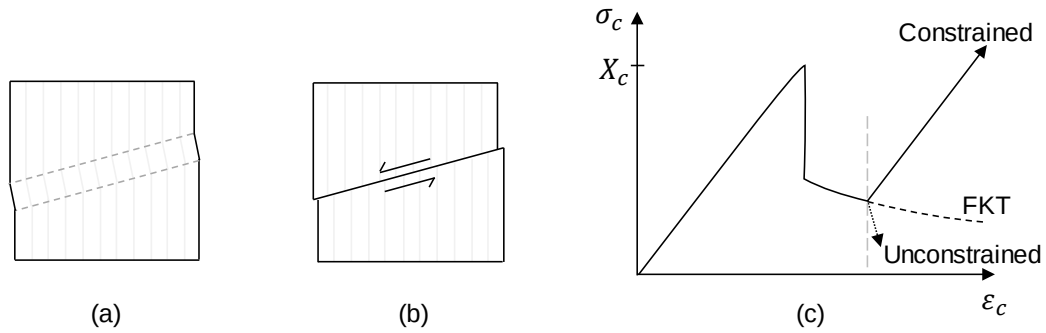

Figure 4. Conceptual model. (a) Fully formed kink band where the dashed grey lines represent the two rows of broken fibers, (b) frictional sliding idealization of the fully formed kink band kinematics, and (c) idealized constitutive response.

segments. Once the fibers have broken and the kink band is fully formed, the material may undergo frictional sliding along the kink band plane, as shown schematically in Figure 4a and b. Considering the constraining effect of neighboring material, the constitutive response in Figure 4c is postulated, where the different constitutive responses that may occur once the kink band is fully formed are shown starting at the vertical gray dashed line in Figure 4c. In the absence of constraint, the material slides along the kinked interface and, for an increment in strain, the stress drops. In contrast, when the local material is highly constrained, sliding along the kinked interface is prevented and the longitudinal stress increases. An intermediate level of constraint corresponds to the idealized case of an infinitely wide kink band, where Budiansky's crush stress is recovered, shown as the curve labeled FKT in Figure 4c.

The fiber-kinking model described in the previous section is augmented with a simple extension to approximate the conceptual response shown in Figure 4c for the constrained case as follows. A critical fiber rotation angle is introduced, φ_{ff}, representing the fiber rotation at which point the fibers break. A corresponding critical plastic strain, $\gamma_{12,c}^{PL}$, is determined using

$$\varphi_{\text{ff}} - \varphi_0 = \gamma_{12,c} \tag{16}$$

where the subscript c denotes the critical value where the fibers break. Substituting equation (8) in to (16) and rearranging results in

$$\gamma_{12,c}^{PL} = \varphi_{\text{ff}} - \varphi_0 - \gamma_{12,c}^{EL} \tag{17}$$

which is solved using (9). The critical plastic strain is the maximum plastic strain allowed.

$$|\gamma_{12}^{PL}| \leq \gamma_{12,c}^{PL} \tag{18}$$

Thus, fiber failure occurs when $|\gamma_{12}^{PL}| = \gamma_{12,c}^{PL}$ which corresponds to $|\varphi| = \varphi_{\text{ff}}$. By arresting further change in the plastic strain at φ_{ff}, the constitutive response shown in Figure 4c is approximated. It is emphasized that the model reproduces the constitutive response in Figure 4c without consideration for $\beta > 0$ and frictional sliding. Instead, the plastic strain is manipulated artificially. An implication of this approach is that, once $|\varphi| \geq \varphi_{\text{ff}}$ is satisfied, the kinematics and plastic strain are no longer physically meaningful. Nonetheless, the model appears to be a reasonably good approximation of

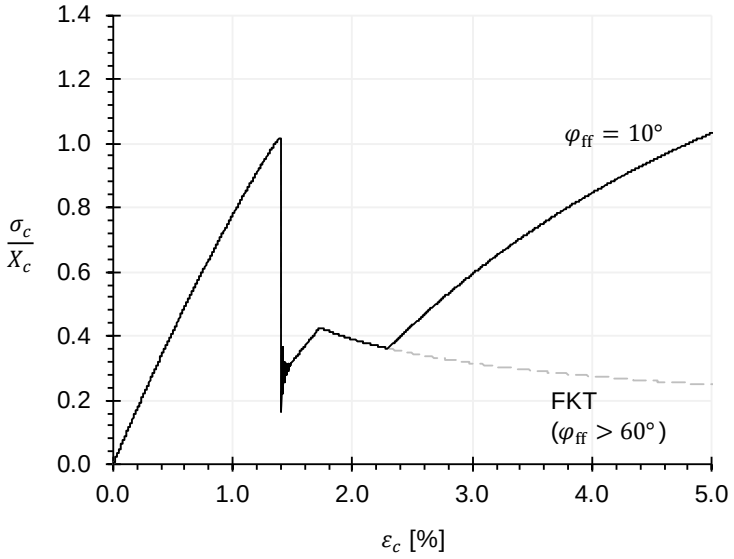

Figure 5. Stress vs. strain with and without fiber failure.

the conceptual response described in Figure 4a and b as discussed in the remainder of the paper.

A single element analysis demonstrates the stress vs. strain response yielded by the proposed model. The case where the fiber failure angle is set to a large angle (i.e. fiber failure is disabled) is shown in Figure 5 as a grey dashed line and corresponds to the previous model implementation and FKT. With the fiber failure angle $\varphi_{\text{ff}} = 10°$, the model yields the stress-strain curve shown as the solid black line in Figure 5, which is a very good approximation of the 'constrained' curve in Figure 4c. There is an overshooting behavior for both curves as the stress drops sharply after the strength is reached as a result of dynamic effects. The sudden increase in stress at around 2.3% strain is due to activation of the fiber failure criterion which prevents further accumulation of plastic strain. The stress increases beyond the original strength, which enables the model to predict band broadening. The smooth nonlinearity of the stress vs. strain curve for $\varepsilon_c > 2.3\%$ is due to large rotation of the fiber axis.

A more sophisticated constitutive model would predict the effect of constraint and recover any of the three potential responses shown Figure 4c as appropriate. However, since the notch tip condition in the DENC specimens is characterized by the constrained condition, the approximation described here is adequate.

DENC Model

The fiber-kinking model is applied to predict the response of the DENC specimens in order to validate the accuracy and representativeness of the fiber-kinking model. The details of the finite element model of the DENC specimen are described in this section.

A reduced thickness DENC specimen modeled with seven plies was developed as shown in Figure 6. The rationale for choosing to model seven plies was based on three considerations: 1) reducing the model size to decrease the run time, 2) maintaining 90° plies on the exterior since the damage response for surface plies, where one side of the ply is unsupported, is often different than the damage response of internal plies, and 3) capturing the potential for interaction between kinking in multiple 0° plies. The ply thicknesses were scaled proportionally so that the modeled laminate thickness, t_M, is

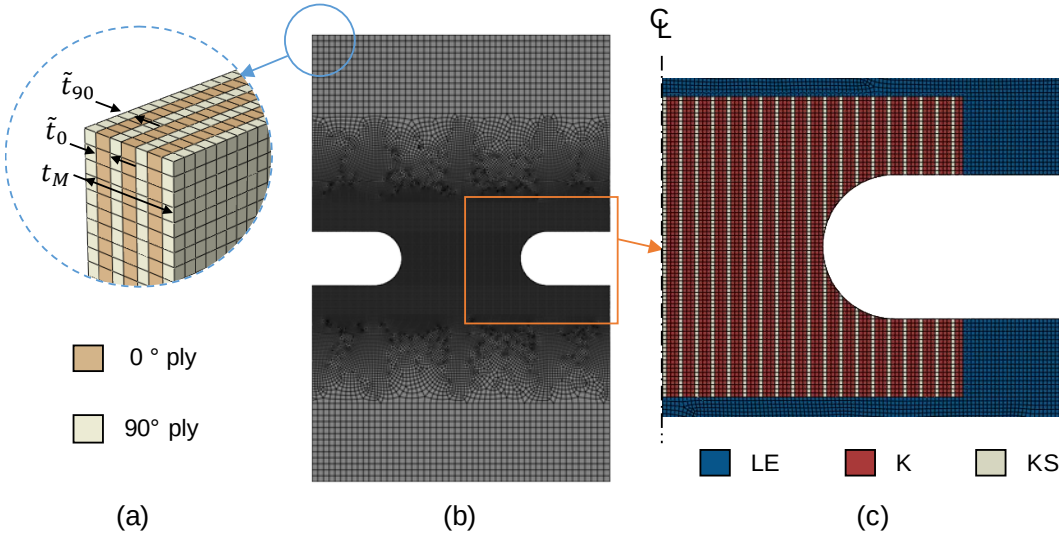

Figure 6. Typical mesh (a), (b) and (c) section assignments used for modeling the DENC specimens. The section assignments are denoted 'LE' for linear elastic, 'K' for kinking enabled, and 'KS' for kinking and splitting enabled. Size A shown.

one fourth of the laminate thickness, $\bar{t} = t_L/t_M = 4$, and the ratio of the thicknesses of the 0° and 90° plies (t_0/t_{90}) is the same in the test specimen and the model. In the general case, for the number of 0° plies and 90° plies in model $\tilde{n}_0$ and $\tilde{n}_{90}$, respectively, the scaled ply thicknesses in the model ($\tilde{t}_0$ and $\tilde{t}_{90}$) are given as

$$\tilde{t}_0 = \frac{n_0}{\tilde{n}_0}\frac{t_{\text{ply}}}{\bar{t}} \tag{19}$$

$$\tilde{t}_{90} = \frac{n_{90}}{\tilde{n}_{90}}\frac{t_{\text{ply}}}{\bar{t}} \tag{20}$$

where n_0 and n_{90} are the actual number of 0° and 90° plies in the test specimen laminate, respectively. Each ply is modeled with a fiber-aligned mesh consisting of one layer of solid continuum elements with reduced integration (C3D8R) and enhanced hourglass control. Fiber kinking is enabled only in the region near the notches where damage is expected to occur, as shown in Figure 6c. The material properties given in Table II were used. Fiber nonlinearity was considered with $c_l = 10$. Zero-thickness cohesive elements (COH3D8) were used at each ply interface in the region where damage is enabled to allow for delamination during the analysis. The properties used for the cohesive elements are listed in Table III. In some cases, the model included progressive intralaminar matrix damage in the 0° plies to model splitting cracks. In these models, a crack spacing was enforced through the section assignments with three elements that are not allowed to crack between each row of elements that could potentially develop matrix cracks [13]. This alternating section definition yields a minimum crack spacing is 0.2 mm, as shown in Figure 6c. Damage in the 90° plies was ignored in the simulations based on the assumption that the 0° plies dominate the response. The finite element models were generated using the Abaqus Python Scripting Interface [11]. Three of the nine test specimen sizes were analyzed.

The typical element size $l_e = 0.05$ mm was used in the notch tip region where damage was enabled. This mesh size was chosen for mesh convergence of the

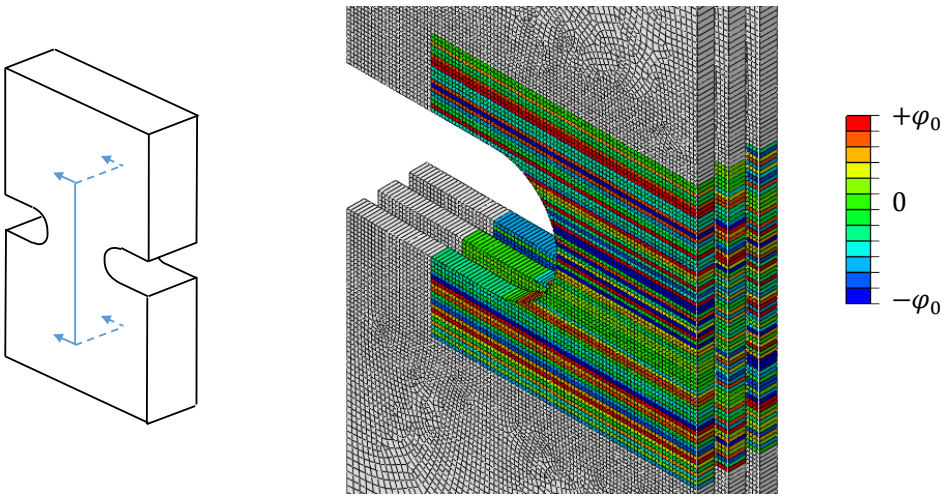

Figure 7. Initial fiber misalignments (only showing the 0° plies). Size A shown.

lonitudinal stress field near the notch tip. Since this mesh size is on the order of the kink-band width w_{kb} reported in the literature for IM7/8552 [5], and the model requires $l_e \geq w_{\mathrm{kb}}$, it was assumed that $w_{\mathrm{kb}} = l_e = 0.05$ mm. Uniform end shortening was applied to the face where $y = h$ and the opposite face was constrained in the y-direction. The analysis was performed using Abaqus/Explicit with two steps, each 0.1 seconds in duration. Two steps were used in order to take advantage of the computational speed up afforded by large mass scaling during loading prior to damage initiation in the first step (typical mass scaling factor = 10^5). In the second step, where damage initiates and propagates, much less mass scaling is utilized (typical mass scaling factor = 10^3) such that the kinetic energy is negligible. The actual mass scaling was determined during the analysis based on element size and stiffness via the automatic mass scaling feature in Abaqus [11].

The initial misalignments were introduced by the model prior to starting the analysis using a random uniform distribution and the VEXTERNALDB subroutine. The distribution spans the range $[-\varphi_0, \varphi_0]$ where $\varphi_0 = 1.15°$ is obtained from (5). The misalignment wave length was not included such that the most severe misalignment was from a large negative to large positive angle in adjacent elements. The variation in the initial misalignment occurs in the fiber direction only. Each 0° ply is seeded with a different set of initial misalignments, as shown in Figure 7. Though the model is capable of quantifying the uncertainty due to the initial fiber misalignment through analyzing several realizations, only one realization was considered here. While the misalignment

TABLE II. IM7/8552 PLY PROPERTIES.

E_1 (MPa)	E_2 (MPa)	G_{12} (MPa)	ν_{12}	ν_{23}	α (MPa$^{1-\eta_{\mathrm{PL}}}$)	η	X_C (MPa)
152,689	8703	5164	0.32	0.45	4.06×10^{-9}	5.4	1731

TABLE III. IM7/8552 INTERFACE PROPERTIES.

N (MPa)	S (MPa)	G_N^c (kJ/m^2)	G_S^c (kJ/m^2)	η_{BK}
80.1	97.6	0.24	0.739	2.07

realizations were consistent within each specimen size, they differed among the different specimen sizes.

RESULTS

Selected results from the test and analysis campaign are provided and discussed in this section. Details regarding the correlation of the analysis predictions with test observations are discussed in terms of the overall structural response and the evolution of damage throughout loading.

Structural Response

The overall structural responses for two sizes, A and E, are shown in Figure 8. The compressive displacement, Δ_c, was measured in the tests using the DIC systems between two far field points with an initial separation of $0.75h$ along the centerline of the specimen, $x = w$. The DIC data from the front surface and back surface were similar and are averaged together and shown as grey dashed lines. Black cross symbols are shown where the maximum load was recorded in the test. The average maximum load for the size A and E specimens was 15.4 kN and 36.7 kN, respectively. After the maximum load was reached, a dynamic failure event occurred where damage propagated and connected the two notch tips. Prior to reaching the maximum load, evidence of kinking in the 0° plies was visible on the notch surfaces. The visual observations of kinking were recorded and are shown in Figure 8 as the grey circles. The first visual indication of fiber kinking in the test occurred at 12.7 kN and 28.8 kN for sizes A and E, respectively. Solid black lines labeled 'Linear' were fit through the initial linear portion of the test data to show the nonlinearity in the load vs. displacement curve that develops prior to collapse.

The corresponding analysis results for specimens A and E are overlaid on the test data in Figure 8 in order to evaluate the correlation with test data. Analysis results are

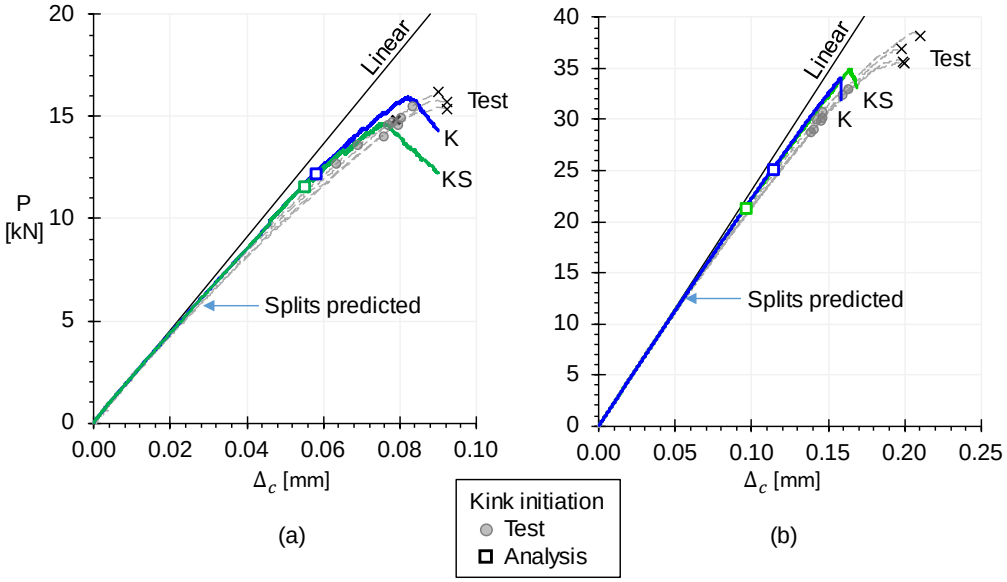

Figure 8. Load vs. displacement response from test and analysis for specimens: (a) size A and (b) size E.

shown for models with splitting (green line) and without splitting (blue line), and labeled as 'KS' and 'K', respectively. The analysis results are truncated when the kinetic energy exceeds 1% of the strain energy since dynamic effects dominate the response after this point. The peak loads predicted by the analysis without splitting cracks were 15.9 kN and 34.1 kN, for sizes A and E, respectively. In the case when splitting cracks were enabled, the peak loads were 14.7 kN and 34.9 kN, for sizes A and E, respectively. For both models, the point where kinking initiates is shown with a square symbol. Likewise, the load level at which splitting damage initiated is annotated on the plots.

Overall, the correlation between test and analysis for the load vs. displacement response is excellent in terms of stiffness and strength. The analysis captured the pre-peak nonlinearity observed in the test. While the initiation of splits in the model occurs at about the point where nonlinearity in the load vs. displacement response becomes apparent, the fact that the analysis results with and without splits are nearly identical suggests that the pre-peak nonlinearity is due to the fiber nonlinearity (c_l) and not the splitting cracks. The analysis predicted the formation of kinks at loads below the experimental observations. The discrepancy was more severe for the size E specimen. However, the test observations were limited to visual observations of the outer surface and therefore kinking may have initiated prior to the first visual evidence. The analysis predicted peak loads that correlate well with the experimental values. Further discussion on the role of splitting in the predicted strength is given below.

The strength of the specimens was obtained by dividing the peak load by the nominal cross sectional area. The results for strength as a function of the specimen size, w, are shown in Figure 9. The test data were fit with a size effect law (SEL). The predicted values for strength are in good agreement for sizes that were analyzed: A, E, and I. The analysis with kinking and splitting (KS) has a maximum error compared with the test average of 8.4% for size I compared with the test average. It is interesting to note that the relative significance of the splitting cracks on the ultimate strength predicted by the model appears to diminish with specimen size.

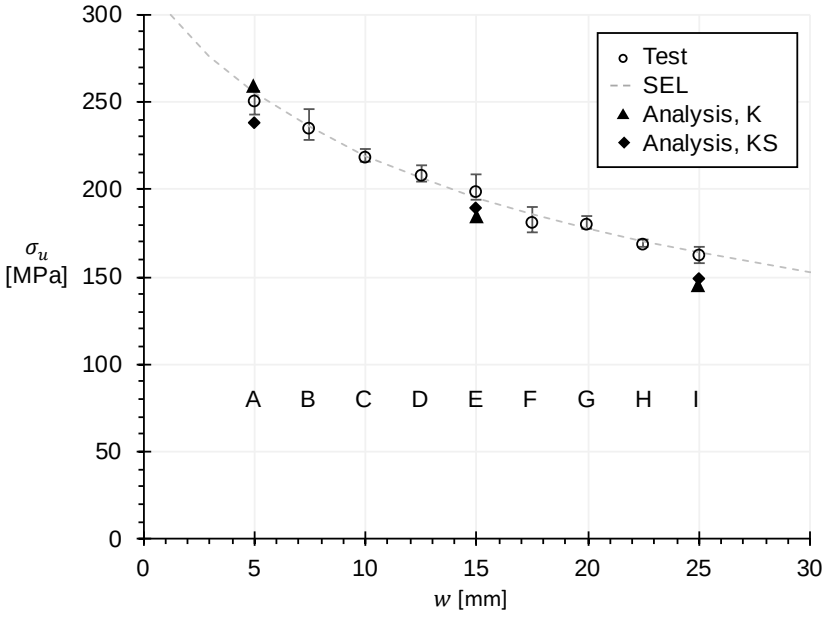

Figure 9. Strength vs. size from test and analysis.

Sequence of Damage Events Leading to Collapse

The model of the DENC specimen predicted a sequence of five events leading up to the collapse. The same sequence of events was predicted for all specimen sizes. This section discusses these events and makes correlations with test observations where available. The five events are summarized in Table IV, including load levels for the size E specimens. Where the models with and without splitting exhibited the events at different load levels, the load levels for both models are given and identified with K and KS.

The first event, splitting and plasticity at the notch tip, occurs relatively early on, at around 34% of the strength for size E. In the case when splitting cracks were enabled in the analysis, they initiate and grow to a length of about 1 mm through the course of loading. In the case when splitting cracks were disabled, significant plasticity occurs near the notch tip at the same location as where splitting cracks would have formed had they been enabled. In both cases, these nonlinearities near the notch tip occur prior to kinking and have an impact on the local stress distribution. While no observations of splitting cracks were recorded in the tests reported herein, this mode has been observed to precede kinking [14,15].

The second event is the initiation of kinking. As mentioned previously, the analysis predicts kinks to initiate before they are first visible in test observations. In both cases, the location of kink initiation is offset from the center of the notch tip ($y = h/2$), where the maximum compressive stresses occur. Kinks initiate in the region of high compression and shear stresses, as shown in Figure 10. In the figure, the longitudinal compressive stresses are shown with the colored contour plot. A single contour line

TABLE IV. SEQUENCE OF EVENTS IN TEST AND ANALYSIS (LOADS FOR SIZE E).

Event	Description	Analysis load range [kN]	Test load range [kN]
1	Splits initiate; significant plasticity at notch tip when splitting disabled	~ 12	N/A
2	Kinks initiate	25.1 (K) 21.4 (KS)	28.8 [a]
3	Additional kinks initiate as load redistributes	25.1 – 33.2 (K) 21.4 – 32.6 (KS)	28.8 – 36.9 [b]
4	Kinks drive delamination growth	25.1+ (K) 21.4+ (KS)	N/A
5	Large delaminations lead to buckling of plies resulting in collapse of the specimen	34.1 (K) 34.8 – 34.9 (KS)	34.5 [a]

[a] Specimen E-1 only, peak load = 37.0 kN

[b] Range recorded for all E specimens

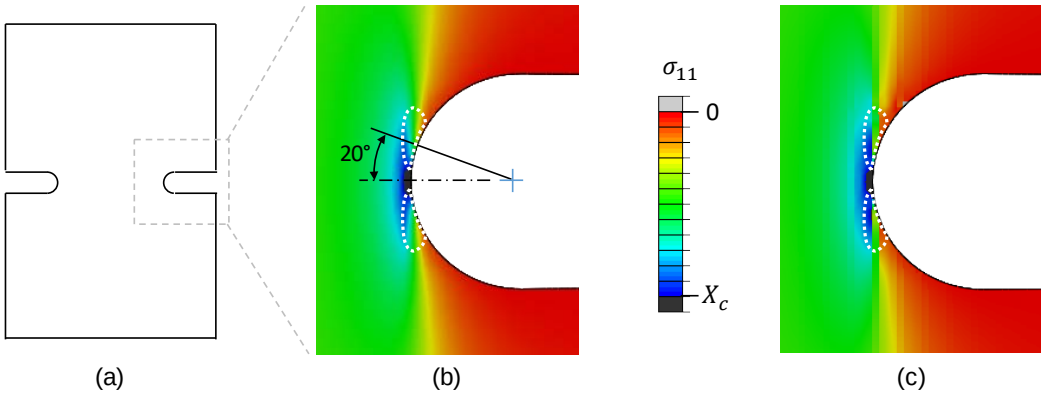

Figure 10. Longitudinal stress distribution in a 0° ply just prior to initiation of kinking. (a) Schematic of specimen showing location of the inset views with (b) splitting disabled and (c) splitting enabled. Size A.

(white, dotted line) highlighting the regions of highest shear stress are overlaid. The area where the high compression and shear stresses coincide is located at about 20° from the x-direction. Kinks initiate in this location. As can be observed from Figure 10, splitting cracks have an effect on the longitudinal stress distribution, but they do not change the location of kink initiation.

After the first kink band forms, additional kinks form in the other 0° plies and ahead of the other notch tip such that, eventually, all of the 0° plies have kink bands propagating from the two notch tips. The accumulation of kink bands is driven by stress redistribution. The first kink band to initiate occurs in the 0° ply with the most severe initial misalignment near the location of high compression (σ_{11}) and high shear stresses (σ_{12}). After the kink band forms, the compressive stress redistributes to the neighboring 0° plies, which eventually also begin to kink. Likewise, kinking initiates at one notch tip, and then, shortly afterward, kinking occurs at the opposite notch tip. The test observations clearly confirmed this sequential accumulation of kinks in the 0° plies. A side-by-side comparison of kink band accumulation in the test and analysis is shown in Figure 11a and b, for load levels just after kink bands initiate. The analysis results show the location of kink bands in red. As the last few kink bands form, the existing kink bands grow in two directions: 1) through crack-like propagation in a direction transverse to the loading and 2) through band broadening, along the loading direction. The kink band propagation behavior is shown with the white arrows in the analysis result in Figure 11b. No observations of kink band propagation were possible using the test data since only observations on the outer surface were recorded. The only observations available from the test are shown in Figure 11b, where further accumulation of kinks is noted.

The model results indicate that the kinks create delaminations. The delaminations initiate at the same load level as the kinks and grow along with the kinks. Once the delaminations become large enough, the 0° plies begin to buckle, which opens the delaminations and leads to collapse of the specimen. Out-of-plane displacement, u_z, provides an indication of this sublaminate buckling event that occurs just prior to collapse. Contour plots of u_z from test and analysis are in very good agreement, as shown in Figure 11c.

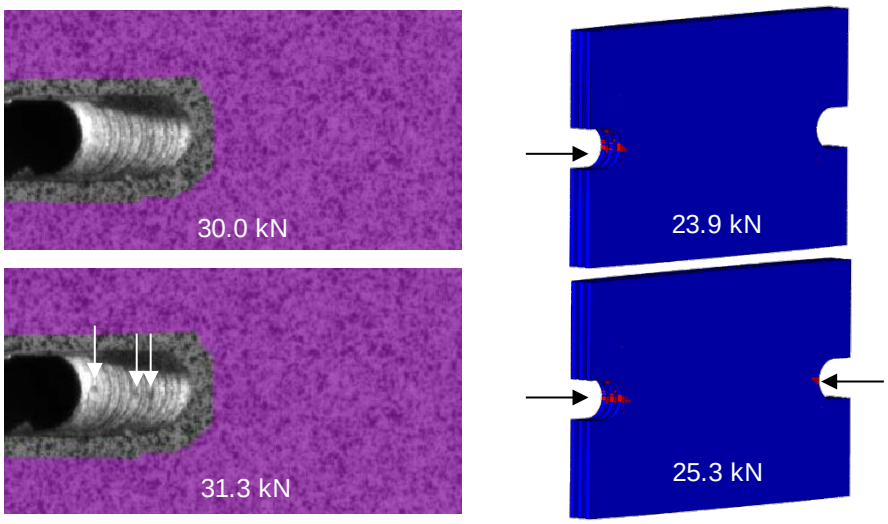

a) kinking initiation

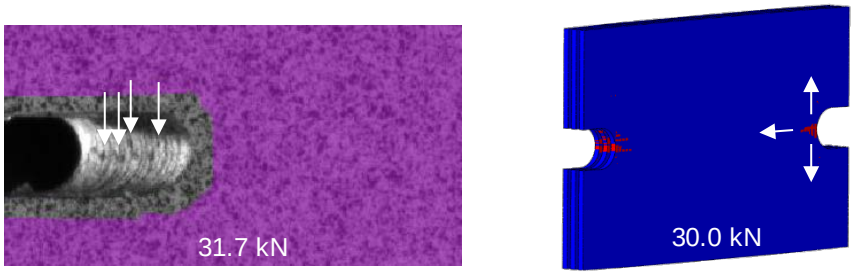

b) kinking propagation

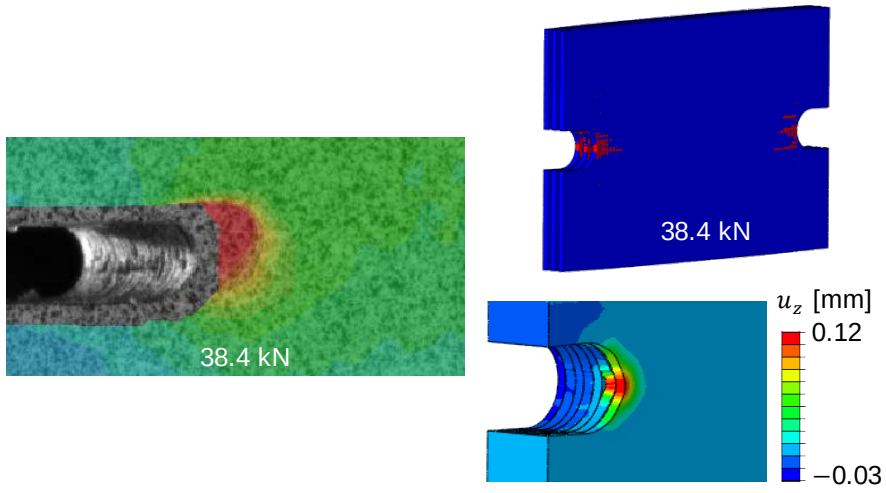

c) Just prior to collapse

Figure 11. Typical evolution of kink bands observed in test (left column) and analysis (right column). Analysis results show kinks in red. Evidence of kink bands observed during testing are labeled with white arrows.

CONCLUDING REMARKS

A validation study for longitudinal compression failure of a carbon epoxy reinforced polymer was described in this paper. Test data for validation of the model was generated from a test campaign of geometrically scaled double edge notch compression specimens. Nine different specimen sizes were loaded quasi-statically to failure. Full-field displacements were monitored and recorded using three digital image correlation systems.

A previously-developed material model for predicting fiber kinking at the ply-level was extended to account for the hardening in the constitutive response after a kink band has fully formed. The behavior of a fully formed kink band is modeled by holding the plastic strain constant once a criterion based on fiber rotation is satisfied. A verification study with a single-element model demonstrated that the constitutive response produced by the model approximates the conceptual model of fully formed kink bands under constrained conditions.

Correlations between the test observations and analysis results are examined in terms of load vs. displacement response and the sequence of events leading to ultimate failure in order to validate the capability of the model. The agreement in terms of stiffness and strength are excellent for the range of specimens tested. Examination of the failure process shows that the test and analysis predict the same sequence of events and the load levels at which the events occur are in good agreement. The role of matrix splitting cracks in the 0° plies was examined and found to affect the ultimate strength. The overall excellent correlation in terms of stiffness, strength, and failure process validates the capability of the model for predicting longitudinal compression failure in notched laminates with cross-ply layups. Furthermore, the correlation between test and analysis demonstrates the ability of the model to predict size-effects.

ACKNOWLEDGEMENTS

The authors wish to acknowledge the contributions of Mr. Michael O'Neil, Dr. Nathaniel Gardner, and Dr. David Dawicke in collecting and processing the DIC data.

REFERENCES

[1] A. Matzenmiller, J. Lubliner, and R. L. Taylor. 1995. "A Constitutive Model for Anisotropic Damage in Fiber-Composites," *Mech. Mater.*, 20(2):125–152.

[2] P. Maimí, P. P. Camanho, J.-A. Mayugo, and C. G. Dávila. 2006. "A Thermodynamically Consistent Damage Model for Advanced Composites," NASA/TM-2006-214282, Hampton, VA.

[3] B. Budiansky. 1983. "Micromechanics," *Comput. Struct.*, 16(1):3–12.

[4] B. Budiansky and N. A. Fleck. 1993. "Compressive Failure of Fibre Composites," *J. Mech. Phys. Solids*, 41(1):183–211.

[5] A. C. Bergan, M. Herráez, C. González, and C. S. Lopes. 2018. "Development of a Mesoscale Finite Element Constitutive Model for Fiber Kinking," presented at the 59th AIAA/ASCE/AHS/ASC Structures, Structural Dynamics, and Materials Conference - SciTech, Kissimmee, FL, January 8-12, 2018.

[6] G. Catalanotti, J. Xavier, and P. P. Camanho. 2014 “Measurement of the Compressive Crack Resistance Curve of Composites Using the Size Effect Law,” *Compos. Part Appl. Sci. Manuf.*, 56:300–307.
[7] B. Budiansky, N. A. Fleck, and J. C. Amazigo. 1998. “On Kink-Band Propagation in Fiber Composites,” *J. Mech. Phys. Solids*, 46(9):1637–1653.
[8] W. Ramberg and W. R. Osgood. 1943. “Description of Stress–Strain Curves by Three Parameters,” National Advisory Committee for Aeronautics, Technical Note No. 902, Washington, DC.
[9] F. A. Leone Jr., A. C. Bergan, and C. G. Dávila. 2019. “CompDam_DGD Version 2.0.2.” GitHub repository, [Online]. Available: https://github.com/nasa/CompDam_DGD.
[10] I. Kowalski. 1998. “Characterizing the Tensile Stress-Strain Nonlinearity of Polyacrylonitrile-Based Carbon Fibers,” presented at the Eight Conference on Composite Materials: Testing and Design, Philadelphia, PA.
[11] *ABAQUS Online Documentation: Version 2017*. Dassault Systèmes SIMULIA Corporation, Providence, RI.
[12] R. Gutkin, S. T. Pinho, P. Robinson, and P. T. Curtis. 2010. “On the Transition from Shear-Driven Fibre Compressive Failure to Fibre Kinking in Notched CFRP Laminates Under Longitudinal Compression,” *Compos. Sci. Technol.*, 70(8):1223–1231.
[13] I. Hyder, F. A. Leone Jr., B. P. Justusson, J. D. Schaefer, A. C. Bergan, and S. Wanthal. 2018. “Implementation of a Matrix Crack Spacing Parameter in a Continuum Damage Mechanics Finite Element Model,” presented at the American Society for Composites 33rd Technical Conference, Seattle, WA, September 24-26, 2018.
[14] A. C. Bergan and S. C. Garcea. 2017. “In-Situ Observations of Longitudinal Compression Damage in Carbon- Epoxy Cross Ply Laminates Using Fast Synchrotron Radiation Computed Tomography,” presented at the American Society for Composites 32nd Technical Conference, West Lafayette, IN, October 22-25, 2017.
[15] The Boeing Company. 2016. “Advanced Composites Project for Certification Timeline Reduction,” NASA/CR-2016-NNL10AA05B, Hampton, VA.